PHYSICAL REVIEW C **69**, 024610 (2004)

Double folding nucleus-nucleus potential applied to heavy-ion fusion reactions

I. I. Gontchar,[*] D. J. Hinde, M. Dasgupta, and J. O. Newton
Department of Nuclear Physics, Research School of Physical Sciences and Engineering, Australian National University,
Canberra ACT 0200, Australia

(Received 12 August 2003; published 26 February 2004)

Double folding model calculations to obtain the bare nucleus-nucleus potential have been carried out with the Reid and Paris M3Y effective nucleon-nucleon (*NN*) interactions. The exchange part of the interaction was taken to be of finite range and the density dependence of the *NN* interaction was accounted for. The calculated fusion barrier energies are generally lower than those expected taking into account potential renormalization due to coupling to collective states at high excitation energies. Fitting the potentials at the barrier radii with a Woods-Saxon form results in effective potential diffuseness of ~0.65–0.70 fm, smaller than the values of ~1 fm generally found from fitting fusion cross sections at above-barrier energies. These discrepancies raise questions about both the determination of the bare nucleus-nucleus potential with the folding model, and the boundary of the effect of friction on the fusion process.

DOI: 10.1103/PhysRevC.69.024610 PACS number(s): 25.70.Jj

I. INTRODUCTION

Many nuclear reaction processes are described using the nucleus-nucleus potential, which is often one of the most important ingredients. In particular in the simplest picture of nuclear fusion, the single-barrier penetration model (SBPM), the fusion barrier alone determines the fusion process, and its height, radius, and thickness are determined by the nuclear and Coulomb potentials. Since the latter can be exactly defined, the only uncertainty is in the nuclear potential.

This simple picture is modified when the couplings to vibrational, rotational, and nucleon transfer degrees of freedom are taken into account. As a result of the couplings, the single barrier can be thought of as splitting into a distribution of barriers with different energies and radii [1]. The results of approximate or exact coupled-channels (CC) calculations which model these effects show enhancement of fusion cross sections below the uncoupled single barrier, resulting from the distribution of barrier energies [2]. In the CC model, the nuclear potential still plays a vital role, not only affecting each barrier shape as in the SBPM, but also affecting the coupling strengths, which to first approximation depend on the derivative of the bare (uncoupled) potential. Determination of the bare potential is thus vital in the coupled-channels interpretation of fusion cross sections.

The nuclear potential is often described by a Woods-Saxon form:

$$U_{nWS}(R) = V_{WS}(1 + \exp\{[R - r_{WS}(A_P^{1/3} + A_T^{1/3})]/a_{WS}\})^{-1}. \tag{1}$$

Here R denotes the distance between the centers of mass of the projectile nucleus of mass number A_P and the target nucleus of mass number A_T. The Woods-Saxon potential (WSP) is defined by three parameters: the depth V_{WS}, the radius parameter r_{WS}, and the diffuseness a_{WS}. Different sets of V_{WS} and r_{WS} can give very similar nuclear potential values at a given point in its tail, however the slope of the potential in the tail is determined predominantly by the diffuseness a_{WS}. Since the fusion barrier occurs in the tail of the nuclear potential, one might hope that a_{WS} (but not both V_{WS} and r_{WS}) could in principle be determined from fusion cross section data after accounting for channel coupling effects. An effective nuclear potential (but not the bare potential) was mapped out by Bass [3] from a classical analysis of above-barrier fusion cross sections from a wide range of reactions.

In different bombarding energy regimes, the fusion cross sections have a different sensitivity to the diffuseness of the nuclear potential. The lowest energies correspond to the deep sub-barrier region, below the energy of the lowest barrier. In this energy region the fusion cross sections calculated according to the well-known formula of Ref. [4] depend exponentially on a_{WS} through the barrier curvature. Measurements at such energies are, however, difficult to perform because the cross sections are very low. Also it can be difficult to be certain that the energies are below that of the lowest fusion barrier. The second energy region spans the barrier. Here the shape of the barrier distribution is sensitive to a_{WS}, but it is also sensitive to the couplings, which are not yet sufficiently well known to allow determination of a_{WS}. The third energy region is at above-barrier energies. Up to energies where the pocket in the potential disappears for the highest angular momenta, fusion cross sections can be well described by the classical expression

$$\sigma(E_{\text{c.m.}}) = \pi R_E^2(1 - B/E_{\text{c.m.}}), \tag{2}$$

even in the presence of couplings which increase the cross sections at sub-barrier energies. Here B represents the energy of the average fusion barrier corresponding to zero orbital angular momentum. The effect of angular momentum on the fusion barrier radius is included through the energy dependence of the barrier radius R_E. It was shown [5] that for an exponential form of the nuclear potential, R_E is reduced from

---

[*] Permanent Address: Omsk State Transport University, pr. Marxa 35, Omsk RU-644046, Russia.

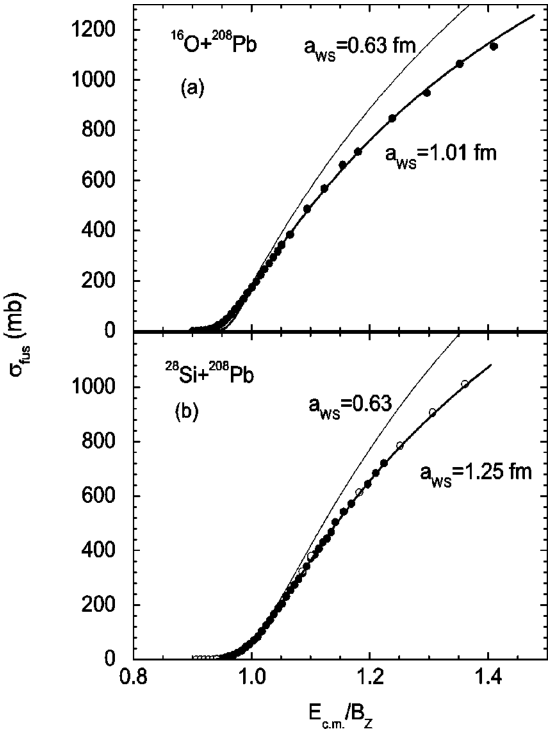

FIG. 1. Measured fusion cross sections compared with those calculated [7] with the coupled-channels code CCMOD, as a function of center-of-mass energy divided by $B_Z = Z_P Z_T/(A_P^{1/3}+A_T^{1/3})$. The data for the $^{16}\mathrm{O}+{}^{208}\mathrm{Pb}$ reaction are from Ref. [7], while those for the $^{28}\mathrm{Si}+{}^{208}\mathrm{Pb}$ reaction are from Ref. [8] and our recent unpublished results (open circles). The experimental data clearly cannot be reproduced with values of a_{WS} close to 0.63 fm.

the zero angular momentum radius R_0 according to the approximate formula

$$R_E \simeq R_0 - a_{WS}\ \ln[(2E_{\mathrm{c.m.}}/B) - 1]. \tag{3}$$

This shows that R_E depends logarithmically on the ratio of the bombarding energy to the barrier energy, but linearly on the diffuseness a_{WS} of the potential.

Thus instead of a linear increase of $\sigma(E_{\mathrm{c.m.}})$ with $1/E_{\mathrm{c.m.}}$, which would occur if $R_E = R_0$, the increase of $\sigma(E_{\mathrm{c.m.}})$ with decreasing $1/E_{\mathrm{c.m.}}$ becomes less steep, depending on the value of a_{WS}. Fitting of $\sigma(E_{\mathrm{c.m.}})$ in the above-barrier region using the SBPM has been carried out for many reactions (see, e.g., Ref. [6]) to determine an empirical value of a_{WS}. This diffuseness has then been used in the coupled-channels calculations. With the recent development of reliable systematics, resulting from the good empirical fits which have been obtained to precise fusion cross sections for a large number of reactions, evidence has built up that the value of a_{WS} extracted by this method is considerably larger than the value of $\simeq$0.63 fm commonly accepted as a typical value that describes elastic scattering [6]. This situation is illustrated by Fig. 1. Here the measured and calculated fusion cross sections are presented as a function of the dimensionless quantity $E_{\mathrm{c.m.}}/B_Z$, where $B_Z = Z_P Z_T/(A_P^{1/3}+A_T^{1/3})$MeV. The data in Fig. 1(a) are from Ref. [7], while those in Fig. 1(b) are from Ref. [8] (solid circles) and our recent (unpublished) measurements (open circles). The data clearly cannot be reproduced with a diffuseness near 0.63 fm.

The elastic scattering data which are fitted with $a_{WS} \simeq 0.63$ fm [9] are sensitive to the nuclear potential at radii larger than that of the fusion barrier. Thus the discrepancy between the relatively small value of a_{WS} extracted from elastic scattering data and the much larger value of a_{WS} required by the fusion data may reflect the fact that the true nuclear potential shape does not follow the WS ansatz. The latter is still commonly used because of its qualitative behavior and mathematical simplicity. A different parametrization has been suggested in Ref. [6], which in principle may resolve this discrepancy, if the nuclear potential were the only relevant physical quantity. However, dissipative effects [10] could be another possible reason for the apparent large value of a_{WS}, distorting the simple potential barrier passing picture.

As part of the investigation of the above discrepancy, we present here semimicroscopic calculations of nucleus-nucleus potentials. The calculated fusion barrier energies are compared with measured values. By fitting a Woods-Saxon form to these potentials at the fusion barrier radii, the equivalent WS diffuseness parameters have been extracted. These are compared with the corresponding experimental quantities determined from fitting above-barrier fusion cross sections for a wide range of fusion reactions.

The double folding model (DFM) was applied to calculate the nucleus-nucleus potential. This model has been widely used in the last 20 years to calculate the first-order term of the real part of the microscopic optical potential for elastic and inelastic scattering of α particles and heavy ions [9,11]. In practice, the strength of the DFM potential is often renormalized by a factor (expected to be greater than unity) to give the best fit to experimental scattering data. This factor is attributed to the higher-order terms [9] which cannot be calculated with the DFM. This point is further discussed in Sec. IV A. In Refs. [9,11], the interacting nuclei generally had ground state matter distributions that were spherically symmetric. In the present paper we restrict ourselves to fusion reactions involving spherical target nuclei. For the reactions we consider, the density overlap at the fusion barrier radius is typically about 1/4 of the central density. Since the M3Y nucleon-nucleon interaction which we use in our calculations is most appropriate for a nuclear density overlap of about 1/3 [9], in this respect the DFM calculations should be suitable. Furthermore, the relatively low density overlap may make the frozen density approximation, implicit in the DFM, at least reasonable.

Although detailed descriptions of the DFM can be found in many papers (see, e.g., Refs. [12,13]), in order to make this paper self-contained we present in Sec. II a short description of the main formulas used. In Sec. III several results from our DFM calculations are compared with those available in the literature, in order to prove the reliability of our newly developed computer code. In Sec. IV we make a comparison of the calculations with the values of the average fusion barrier B and the WS potential diffuseness a_{WS} extracted from the experimental data, and investigate the influence of different options and parameters of the DFP on the calculated quantities. The conclusions are given in Sec. V.

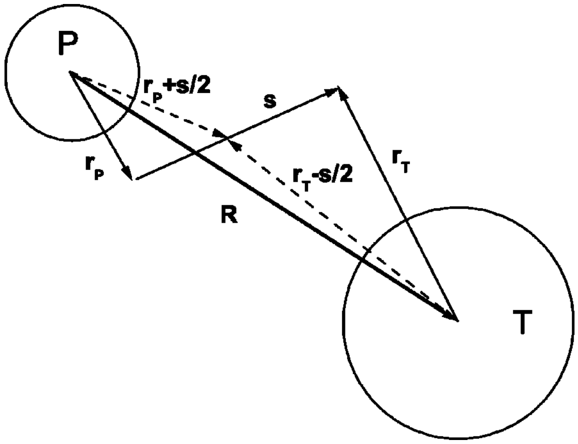

FIG. 2. The coordinate system used in the double folding model. The vector between the centers of the projectile (P) and target (T) nuclei is denoted by $\mathbf{R}$, while $\mathbf{r}_P$, $\mathbf{r}_T$ are the radius vectors of points separated by $\mathbf{s}$ in the nucleon distributions of the projectile and target nuclei.

II. THE DOUBLE FOLDING MODEL

A. The formalism

The interaction potential between two nuclei is written as

$$U(R) = U_C(R) + U_n(R) + U_{rot}(R), \tag{4}$$

where U_C is due to the electrostatic (Coulomb) interaction, U_n is the strong (nuclear) interaction, and U_{rot} is the rotational term. This last term has a very simple structure, and since our purpose here is the calculation of fusion barriers for zero angular momentum, it will not be used here.

The Coulomb energy for two spherical nuclei can be written as

$$U_C(R) = \int d\mathbf{r}_P \int d\mathbf{r}_T \rho_{Pch}(\mathbf{r}_P) v_C(\mathbf{s}) \rho_{Tch}(\mathbf{r}_T). \tag{5}$$

Here ρ_{Pch} and ρ_{Tch} are the charge densities of the projectile (P) and target (T) nuclei, and v_C is the Coulomb interaction. The vector $\mathbf{s}=\mathbf{R}+\mathbf{r}_T-\mathbf{r}_P$ corresponds to the distance between two specified interacting points of the projectile and target, whose radius vectors are $\mathbf{r}_P$ and $\mathbf{r}_T$, respectively. $\mathbf{R}$ denotes the vector joining the centers of mass of the two nuclei. This geometry is illustrated in Fig. 2.

The nuclear part of the potential, U_n, consists of two terms, the direct U_{nD} term and the exchange U_{nE} term, which are in general energy dependent. The direct part of the interaction between two colliding nuclei has a similar form to the equation describing the Coulomb interaction:

$$U_{nD}(R,E_P) = g(E_P) \int d\mathbf{r}_P \int d\mathbf{r}_T \rho_{PA}(\mathbf{r}_P) v_D(\mathbf{s}) \rho_{TA}(\mathbf{r}_T). \tag{6}$$

TABLE I. The coefficients of the Reid and Paris M3Y interactions.

Coefficient	Reid	Paris
G_{D1} (MeV)	7999	11062
G_{D2} (MeV)	−2134	−2537.5
G_{D3} (MeV)	0	0
G_{Ef1} (MeV)	4631.4	−1524.25
G_{Ef2} (MeV)	−1787.1	−518.75
G_{Ef3} (MeV)	−7.847	−7.847
r_{v1} (fm)	0.25	0.25
r_{v2} (fm)	0.40	0.40
r_{v3} (fm)	1.414	1.414
$G_{E\delta}$ (MeV fm^3)	−276	−592
k(MeV^{-1})	0.002	0.003

Here ρ_{PA} and ρ_{TA} are the nucleon densities of the colliding nuclei, v_D is the direct part of the nuclear interaction between two nucleons (*NN* interaction), and $g(E_P)$ is a multiplier that depends upon the energy per nucleon $E_P=E_{lab}/A_P$. The exchange part involves nondiagonal elements of the density matrix (see, e.g., Ref. [12] which we closely follow here):

$$U_{nE}(R,E_P) = g(E_P) \int d\mathbf{r}_P \int d\mathbf{r}_T \rho_{PA}(\mathbf{r}_P;\mathbf{r}_P+\mathbf{s}) \times v_E(\mathbf{s}) \rho_{TA}(\mathbf{r}_T;\mathbf{r}_T-\mathbf{s}) \exp(i\mathbf{k}_{rel}\mathbf{s}/A_{red}). \tag{7}$$

The wave number k_{rel} associated with the relative motion of the colliding nuclei is given by

$$k_{rel}^2(R) = 2m_n A_{red}[E_{\text{c.m.}} - U(R)]/\hbar^2, \tag{8}$$

where the reduced mass number $A_{red}=A_P A_T/(A_P+A_T)$, and m_n is the bare nucleon mass.

Two parametrizations of the nucleon-nucleon interaction in the literature are based, respectively, on the Reid [14] and Paris [15] interactions. These comprise a sum of Yukawa-type terms, known as M3Y effective nucleon-nucleon interactions, comprising both direct v_D and exchange v_{Ef} terms:

$$v_D(s) = \sum_{i=1}^{3} G_{Di}[\exp(-s/r_{vi})]/(s/r_{vi}), \tag{9}$$

$$v_{Ef}(s) = \sum_{i=1}^{3} G_{Efi}[\exp(-s/r_{vi})]/(s/r_{vi}). \tag{10}$$

Here subscript D refers to the direct part of *NN* interaction and the subscript Ef refers to the finite-range exchange part of *NN* interaction. Each term is determined by the radius parameters r_{vi} and the coefficients G_{Di} and G_{Efi}. Instead of a finite-range exchange *NN* interaction, one of zero range was used in early works [9]: $v_{E\delta}(\mathbf{s})=G_{E\delta}\delta(\mathbf{s})$.

The function $g(E_P)$ which defines the energy dependence of the nucleus-nucleus potential in Eqs. (6) and (7) reads [16,17]

$$g(E_P) = 1 - kE_P. \tag{11}$$

The values of all the coefficients, namely r_{vi}, G_{Di}, G_{Efi}, $G_{E\delta}$, and k, are collected in Table I. Unless specified otherwise these values are used throughout this paper. The choice of all

TABLE II. The coefficients of the density-dependent M3Y *NN* interaction of Eq. (12), compiled from Ref. [18].

DD label	Interaction	C	α	$\beta(\mathrm{fm}^{-3})$	$\gamma(\mathrm{fm}^{-3})$
0	D independent	1	0.0	0.0	0.0
1	DDM3Y1	0.2963	3.7231	3.7384	0.0
2	CDM3Y1	0.3429	3.0232	3.5512	0.5
3	CDM3Y2	0.3346	3.0357	3.0685	1.0
4	CDM3Y3	0.2985	3.4528	2.6388	1.5
5	CDM3Y4	0.3052	3.2998	2.3180	2.0
6	CDM3Y5	0.2728	3.7367	1.8294	3.0
7	CDM3Y6	0.2658	3.8033	1.4099	4.0
8	BDM3Y1	1.2521	0.0	0.0	1.7452

the coefficients above is beyond the scope of the present work; we simply follow the prescriptions available in the literature and trace the impact of the values of the coefficients onto the fusion barriers and the value of the equivalent potential diffuseness.

It was widely known that the original density-independent M3Y interaction failed to saturate cold nuclear matter. In order to obtain the correct value of the central nucleon density and nucleon binding energy several versions of a density-dependent M3Y interaction have been proposed (see, e.g., Refs. [16,18]). We use in our study a generalized density dependence of the M3Y interaction introduced in Ref. [18]. It enters as a multiplier $F(\rho_{FA})$ for the density-independent *NN* interaction. The function F is given by

$$F(\rho_{FA}) = C\{1 + \alpha\exp(-\beta\rho_{FA}) - \gamma\rho_{FA}\}. \qquad (12)$$

The nucleon density ρ_{FA} will be specified in the following section. If the M3Y-Paris *NN* interaction is used, this density dependence results in the correct saturation binding energy of about 16 MeV/nucleon and a nuclear density of 0.17 fm^{-3}, for several sets of coefficients that are presented in Table II. The different parameter sets in Table II result in different values of nuclear matter incompressibility, ranging from 176 MeV for the DDM3Y1 interaction up to 270 MeV for the BDM3Y1 interaction. The original density-independent M3Y *NN* forces correspond to parameter set DD0 in this table. The use of density-dependent forces means that the bare M3Y direct and exchange *NN* interactions, $v_D(s)$ and $v_{Ef}(s)$, in Eqs. (6) and (7) should be replaced by

$$\varphi_{D(Ef)}(s,\rho_{FA}) = F(\rho_{FA})v_{D(Ef)}(s). \qquad (13)$$

B. Evaluating the double folding integrals

If a zero-range exchange interaction is used, the integral in Eq. (7) is reduced to that in Eq. (6) and can be easily evaluated. However when finite-range exchange forces are applied, there are two major difficulties in calculating the exchange part of the nuclear potential. First, Eq. (7) with the k_{rel} defined by Eq. (8) results in a self-consistency problem. It is overcome by applying an iterative procedure, which works quite well. Typically from two to ten iterations are needed in order to reach a relative accuracy of 10^{-5} for $U(R)$.

The second obstacle is much more complicated. In order to compute the integral in Eq. (7) one has to calculate the density matrix which depends on two spatial points. The calculation is performed using the density matrix expansion method of Refs. [19,20] which makes the following approximation:

$$\rho_A(\mathbf{r};\mathbf{r}+\mathbf{s}) \simeq \rho_A(\mathbf{r}+\mathbf{s/2})\hat{j}_1(\mathbf{k}_{eff}(\mathbf{r}+\mathbf{s/2})\cdot\mathbf{s}). \qquad (14)$$

Here ρ_A stands for either ρ_{PA} or ρ_{TA} and

$$\hat{j}_1(x) = 3[\sin(x) - x\cos(x)]/x^3. \qquad (15)$$

The simplest way to find the magnitude of the effective Fermi momentum k_{eff} is to apply the Slater approximation where $k_{eff}(r)$ is simply equal to the local Fermi momentum $[3/2\pi^2\rho_A(r)]^{1/3}$. A more sophisticated method, used here, is to calculate k_{eff} using the extended Thomas-Fermi approach [20]:

$$k_{eff}^2(r) = \left(\frac{3\pi^2\rho_A(r)}{2}\right)^{2/3} + \frac{5C_s}{3}\left(\frac{\boldsymbol{\nabla}\rho_A(r)}{\rho_A(r)}\right)^2 + \frac{5\Delta\rho_A(r)}{36\rho_A(r)}. \qquad (16)$$

The only parameter that needs to be specified here is C_s, which defines the strength of the Weizsäcker correction term to the kinetic energy density. In Ref. [17] C_s was taken to be equal to 1/36 whereas in Ref. [12] much larger value of 1/4 was used. Recently in Ref. [11] it was shown that the value of 1/36 provides the best approximation for the exact nondiagonal terms of the density matrix. These terms were obtained in the harmonic oscillator approximation for elastic scattering in the $\alpha + {}^{12}\mathrm{C}$ reaction. Following the prescription of Ref. [11] we use $C_S = 1/36$ when comparing our results with the data.

A further step has to be taken before any calculations of the double folding potential with a density-dependent *NN* interaction can be performed. The nucleon density ρ_{FA} appearing in Eqs. (12) and (13) has to be specified. In Eq. (12) for the direct forces, ρ_{FA} is taken to be equal to $\rho_{PA}(\mathrm{r}_P) + \rho_{TA}(\mathrm{r}_T)$ (see, e.g., Ref. [21]). This choice is dictated more by the numerical convenience than by physical arguments. In Eq. (13), describing the exchange forces, $\rho_{FA} = \rho_{PA}(\mathbf{r}_P + \mathbf{s}/\mathbf{2}) + \rho_{TA}(\mathbf{r}_T - \mathbf{s}/\mathbf{2})$ [12,17,18]. This corresponds to the density at the midpoint between two interacting nucleons and is not merely numerically convenient but also seems to have some physical justification.

In practice when evaluating the double folding integrals (5)–(7) we used the momentum-space representation, closely following Ref. [12]. This dramatically reduces computer time.

C. Charge and nucleon density distributions

Finally, the charge and nucleon density distributions must be specified. In these calculations for simplicity we take the nucleon density to be proportional to the proton density:

$\rho_{P(T)A}=\rho_{P(T)Z}A/Z$. For the proton density distributions $\rho_{P(T)Z}$, two-parameter Fermi (2pF) profiles were used for both projectile and target nuclei:

$$\rho_{P(T)Z}(r)=\rho_{0P(T)}\{1+\exp[(r-R_{P(T)})/a_{P(T)}]\}^{-1}. \qquad (17)$$

The parameters $R_{P(T)}$ and $a_{P(T)}$ were defined using the data on the charge density from Table I of Ref. [22]; these were obtained experimentally from electron elastic scattering. These parameters were used directly to calculate $U_C(R)$. Electron scattering experiments give information on the charge density distribution of the scattering nucleus whereas to calculate $U_n(R)$ in the DFM, the point nucleon density distributions are needed. Therefore the radius parameters for the nucleon density were taken to be equal to those for the charge density whereas the diffuseness parameters were corrected for the finite width of the charge distribution of a single proton. In order to make this correction we used the relation between the average square radii of the proton and charge distributions (see Eq. (17) of Ref. [9]) and the equations relating the average square radius of a 2pF profile with its radius and diffuseness parameters (see Ref. [23]).

For those nuclei where the data were not available in Table I of Ref. [22], the radius parameter was obtained by scaling the parameters of the closest nuclei. The diffuseness of the charge density was taken to be equal to that of the closest nucleus for which it was available. The influence on our results of the diffuseness of the nucleon (proton) density distribution is further discussed in Sec. IV.

III. COMPARISON WITH PREVIOUS CALCULATIONS

It is desirable to check that our new DFM computer code works correctly. This was accomplished by comparing our results with those available in the literature.

We first performed calculations for the $^{16}O+^{16}O$ system at $E_{lab}=160$ MeV. The DFM was applied to calculate the real part of the optical potential for this system in Ref. [12] using the finite-range density-dependent M3Y-Reid interaction with $C_s=1/4$, and with the coefficients $C=0.2845$, $\alpha=3.6391$, $\beta=2.9605\ \mathrm{fm}^{-3}$, and $\gamma=0$ for the density dependence of the *NN* interaction. The coefficient k in the energy dependence [$g(E_P)$ in Eq. (11)] was 0.002 MeV^{-1}. The parameters of the proton (nucleon) distribution were taken from Ref. [24]: $R_{P(T)}=2.525$ fm, $a_{P(T)}=0.450$ fm. The results of our calculations are compared with those of Ref. [12] in Fig. 3. The dotted curve represents the direct part of the nuclear potential, the dashed curve shows the exchange part, and the solid curve indicates the total nuclear potential. The agreement of our calculations with the results read from Fig. 5 of Ref. [12] (open symbols) is very good.

The second comparison presented in Fig. 4 is again for the $^{16}O+^{16}O$ reaction but now at $E_{lab}=250$ MeV with $k=0.003\ \mathrm{MeV}^{-1}$, and with density-dependent Paris forces DDM3Y1 and BDM3Y1 (these correspond to parameter sets DD1 and DD8 in Table II). All other parameters were as in the previous case. Our calculations agree well with those of Fig. 1 from Ref. [25].

The third comparison is for the $^{16}O+^{154}Sm$ reaction. This calculation was reported in Ref. [17]. The value of $C_s=1/36$ and the values of R_P and a_P were as given for the previous case. The deformed target nucleus ^{154}Sm was considered to be spherical with $R_T=5.939$ fm, $a_T=0.522$ fm. In Fig. 5 the calculated ratios $U_{n\delta}/U_{nf}$ corresponding to the M3Y-Paris interaction are compared with those from Table I of Ref. [17]. The agreement of our calculations with those of Ref. [17] is very good.

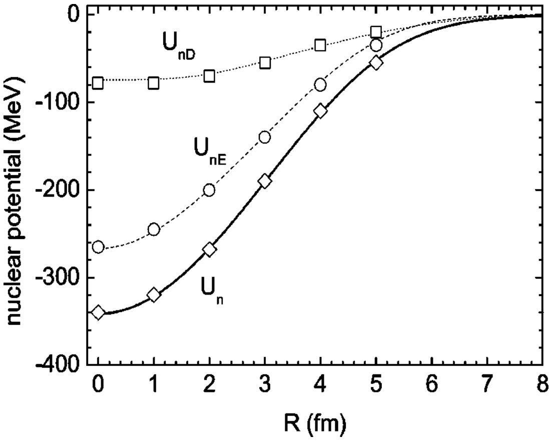

FIG. 3. The total nuclear potential (U_n) and its direct (U_{nD}) and exchange (U_{nE}) components for the reaction $^{16}O+^{16}O$ at $E_{lab}=160$ MeV. The curves represent the present M3Y-Reid calculations (see text) while the open symbols show the values read from Fig. 5 of Ref. [12].

IV. COMPARISON WITH EXPERIMENT

Having checked the validity of our code, the calculated fusion barrier energies and the nuclear potential diffuseness can now be compared with experimental results. Although the primary aim of this work is to investigate the potential diffuseness anomaly, first we show how the different options for the nucleon-nucleon interaction affect the strength of the nuclear potential, and thus the predicted fusion barrier energies. Initially we must consider the effects of channel couplings before making such a comparison.

A. Coupled-channels effect on the fusion barrier energies

Coupling between the relative motion and intrinsic degrees of freedom not only results in a distribution of fusion barrier energies, but can also reduce the average fusion barrier energy, often referred to as potential renormalization [26]. The effect of such potential renormalization should be considered when comparing barrier energies calculated using the DFM with those determined empirically from fitting above-barrier fusion cross sections with a single-barrier model. It has been shown [26] that such potential renormalization can reduce the calculated fusion barrier energies by several percent, so the effect is not insignificant.

In the microscopic optical model, the real potential is the sum of the folded potential and the dynamic polarization potential (DPP) resulting from couplings to excited states. At energies above the barrier region, the DPP is closely related

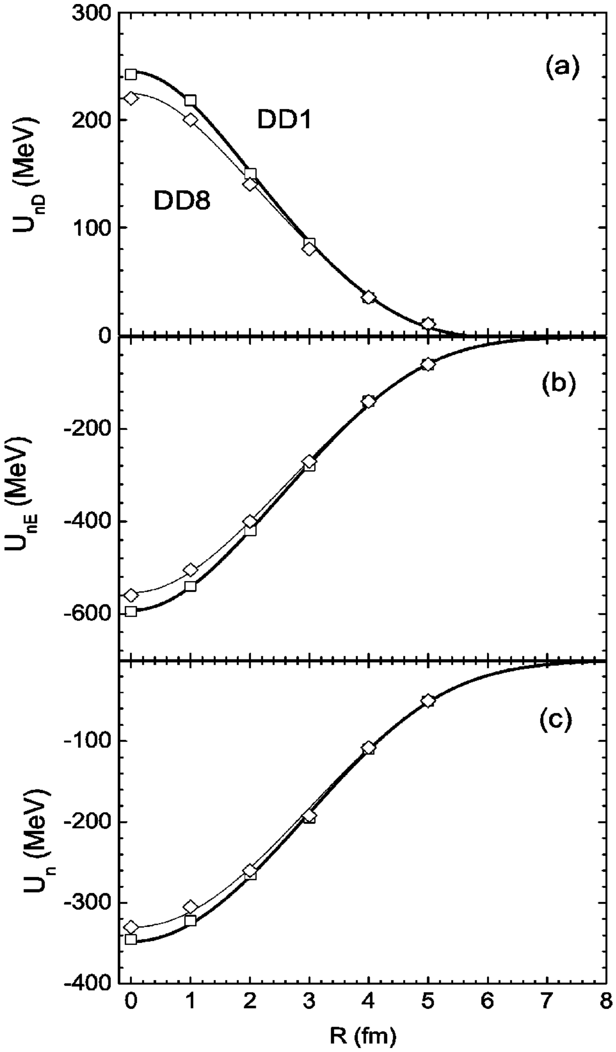

FIG. 4. The total nuclear potential (U_n) and its direct (U_{nD}) and exchange (U_{nE}) components, but for M3Y-Paris interaction including finite-range exchange term, at $E_{lab}=250$ MeV for the ^{16}O $+^{16}$O reaction. The present calculations (lines) are compared with the values (symbols) read from Fig. 1 of Ref. [25] for two different density dependencies (see Table II): DD1 (thick lines, squares) and DD8 (thin lines, diamonds).

to the potential renormalization that is found in the coupled-channels calculations. For the fusion reactions considered here, it acts to increase the attraction of the nuclear potential.

To illustrate the effect of potential renormalization, here we show calculations for the ^{16}O$+^{208}$Pb reaction using the realistic coupled-channels code CCFULL [27]. This is necessary as simplified CC codes based on CCFUS [28], for example CCDEF and CCMOD [29], do not show potential renormalization because of the approximations used [26]. The average fusion barrier energy for the ^{16}O$+^{208}$Pb reaction is 74.5 MeV, determined empirically from a fit with a single-barrier calculation to the above-barrier fusion cross sections. When couplings to the 2.615 MeV 3^- state, the 3.198 MeV 5^- state, and the $3^- \otimes 3^-$ multiplet (in the harmonic limit) in ^{208}Pb are included in the CCFULL calculations, the high energy data can only be fitted using a less attractive nuclear potential, which gives an uncoupled barrier at 75.4 MeV.

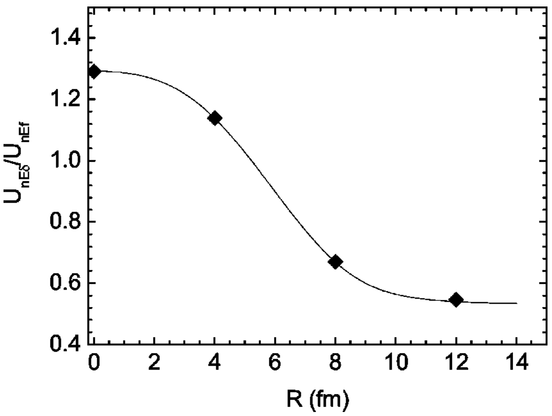

FIG. 5. Calculations for the reaction ^{16}O$+^{154}$Sm at E_P $=5.2$ MeV. The ratio of the zero-range exchange interaction divided by the finite-range interaction for the M3Y-Reid interaction with $C_s=1/36$ is shown; the line corresponds to the present calculations, while the symbols are from Table I of Ref. [17].

Thus the couplings to these collective states not only affect the shape of the barrier distribution, but also shift the barrier by −0.9 MeV. When coupling to the 3^- state at 6.129 MeV in ^{16}O is included in the calculations (in addition to the couplings in ^{208}Pb), then the shape of the fusion barrier distribution is not further changed, but the barrier centroid is shifted to an even lower energy. To compensate for this shift, an uncoupled barrier height of 78.3 MeV is required to obtain a good description of the data. The inclusion of couplings to these projectile and target states therefore effectively reduces the uncoupled barrier height by 3.8 MeV in total. In this calculation, a potential diffuseness of 1.1 fm was used, which was required to fit the above-barrier cross sections, for a potential depth of 300 MeV. The results are illustrated in Fig. 6, where the dotted line shows the single-barrier (uncoupled) calculation with $B=78.3$ MeV, the dashed line shows the effect of including the couplings to ^{208}Pb states, while the full line (with a total energy shift of −3.8 MeV) includes both the couplings to states in ^{208}Pb and that to the 3^- state in ^{16}O. Additional couplings to other high

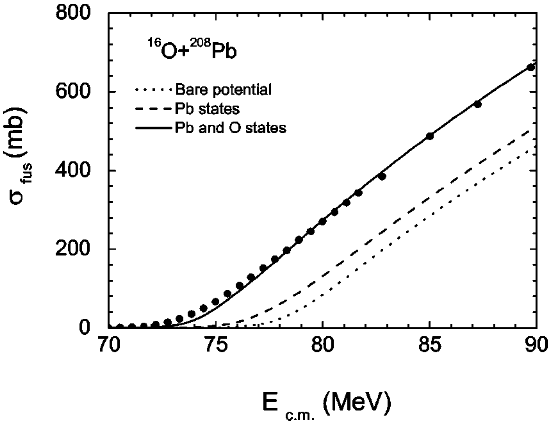

FIG. 6. Calculated and measured fusion excitation functions for the ^{16}O$+^{208}$Pb reaction. The potential renormalization resulting from coupling to high energy states in ^{208}Pb, and more significantly in ^{16}O, is shown (see text).

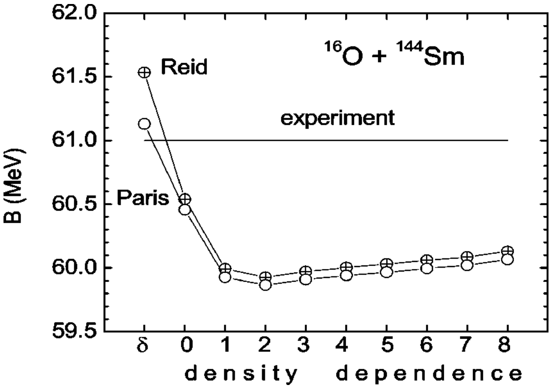

FIG. 7. Calculated fusion barrier energies for the reaction ^{16}O $+ ^{144}$Sm for all types of calculation, namely zero-range (δ) and finite-range density-independent (0) and density-dependent (1–8) interactions. The experimentally determined average barrier energy is indicated by the horizontal line. The open circles correspond to the M3Y-Paris interaction whereas the crossed circles stand for the M3Y-Reid interaction.

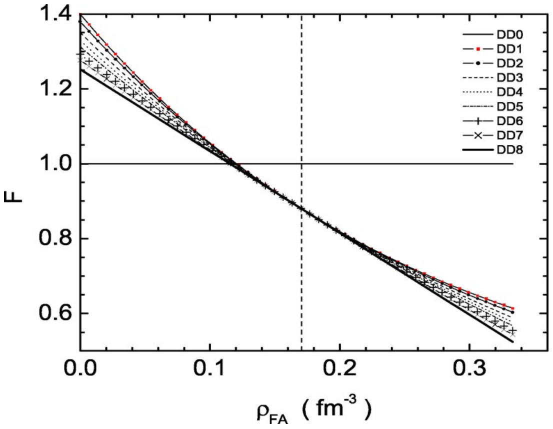

FIG. 8. The dependence of the factor F [which scales the interaction strength, see Eq. (16)] on the nucleon density. The eight curves correspond to the eight sets of coefficients (see Table II). Density-independent forces have $F=1$ (full line). The dashed vertical line shows nuclear saturation density (0.17 fm^{-3}).

energy states, although less strongly coupled than those explicitly included, would be expected to shift the barrier to even lower energy.

Since the effect of couplings is not taken into account in the DFM, the calculated fusion barriers should be considerably higher in energy than the empirical experimental barriers. In the case of ^{16}O$+^{208}$Pb, the fusion barrier calculated with the bare DFM potential should be at least 3.8 MeV(5%) above the experimental value. This is significant, since the contribution of the nuclear potential to the fusion barrier energy is typically less than 10% (e.g., for ^{12}C$+^{92}$Zr it is 7%, as shown in Fig. 12). For reactions of other nuclei, where collective strength may be fragmented over many states, and difficult or impossible to determine experimentally, the exact shift cannot be calculated presently, and further work needs to be carried out on this question. However, it is clear that on average, uncoupled (bare) fusion barriers, such as those calculated with the DFM, should lie several percent above the empirical fusion barrier energies, when potential renormalization (or DPP) is not accounted for.

B. Fusion barrier energies

Since there are several options in the DFM calculations (M3Y-Reid and Paris *NN* interaction, zero- or finite-range interaction, density-dependent and -independent interaction) we first show in Fig. 7 how this choice influences the fusion barrier height. This figure presents barriers calculated for the ^{16}O$+^{144}$Sm reaction, without including potential renormalization due to couplings. These calculations have been performed with the M3Y-Paris (open circles) and Reid (crossed circles) interactions with a zero-range (δ) and with a finite-range (f) exchange term for density-independent interactions, and for all eight versions of the density dependence from Table II. The experimental fusion barrier is shown by the horizontal line.

One sees that changing from zero to finite-range exchange interaction reduces the calculated barrier energies. Indeed, the exchange part of the nucleus-nucleus potential resulting from M3Y *NN* interaction is attractive in both the Reid and Paris potentials (see Figs. 3 and 4). Increasing the range of this attraction from zero to any finite value should only make the fusion barriers lower, which is the case in Fig. 7.

Including the density dependence into the *NN* interaction brings the fusion barrier energy further down in Fig. 7. In order to understand why it happens, it is useful to show the dependence of the potential scaling factor F on the nucleon density, and the density overlap at the fusion barrier. The former is presented in Fig. 8, for all eight density dependence parameter sets in Table II. The horizontal line corresponds to density-independent *NN* interaction. The vertical dashed line indicates the average nuclear central density. The generalized density dependence of Eq. (12) reduces the nucleon-nucleon interaction for large density (around and above nuclear density). For lower values of the density (less than 0.11 fm^{-3}), the density dependence increases the nucleon-nucleon attraction since $F>1$.

Figure 9 shows that the typical minimum density in the region of the density overlap at the barrier is not more than 0.04 fm^{-3} for the reactions considered in this work. In this figure the barrier radii correspond to the M3Y-Reid zero-range interaction. Accounting for the finite range as well as for the density dependence of the interaction makes the barrier radii 2–4% larger thus leading to smaller density overlap. Consequently, the fusion barrier height would be expected to decrease due to the density dependence of the *NN* potential. This is really the case in Fig. 7: the strongest density dependencies labeled 1,2,3 in Table II bring the fusion barrier down to its minimum value among all presented in this figure. The somewhat weaker density dependencies DD4-DD8 result is slightly higher fusion barrier energies, as seen in Fig. 7.

Since the density-independent *NN* interaction was shown to fail in reproducing the basic properties of nuclear matter, we have chosen the density-dependent Paris *NN* interaction with finite-range exchange term (CDM3Y3) for the systematic comparison with the experimental data. Choosing another density dependence of the *NN* interaction will not alter

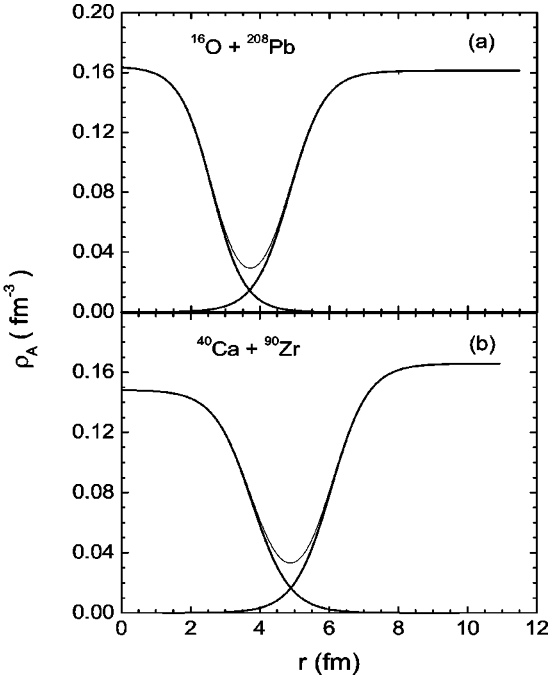

FIG. 9. Individual (thick lines) and total (thin lines) nucleon density distributions at the fusion barrier radii calculated with the M3Y-Reid zero-range interaction for the indicated reactions.

the conclusions of this paper. With this aim the DFM calculations have been performed for the reactions listed in Table VII, for which average fusion barrier energies have been determined experimentally, typically with an accuracy estimated to be better than 0.5%. In order to illustrate the degree of agreement between calculated and experimental barrier energies, both are plotted in Fig. 10(a) versus $B_Z = Z_P Z_T/(A_P^{1/3}+A_T^{1/3})$MeV. The calculated barriers are shown by open circles. Solid circles connected by thin lines represent the experimental barriers. The thick solid line represents $B=B_Z$. The agreement of the calculated barriers with experiment appears to be good, even in detail. These barrier energies are also given in Table VII, where closer inspection shows that the calculated Paris CDM3Y3 barriers are, except for four points, lower than the experimental ones.

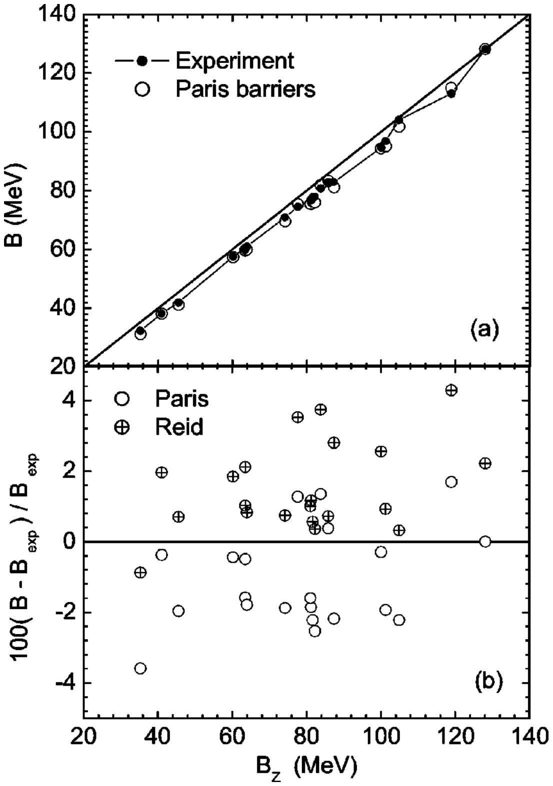

FIG. 10. (a) Fusion barrier energies B vs $B_Z = Z_P Z_T (A_P^{1/3}+A_T^{1/3})$. (a) Filled circles show the experimentally determined barriers, open circles show the calculated Paris CDM3Y3 barriers while the thick line represents $B=B_Z$. (b) Percentage difference between the calculated M3Y-Paris (open circles) and Reid zero-range (crossed circles) barriers, and the experimental fusion barrier energies.

Figure 7 shows that the maximum barrier energies result from the density-independent M3Y-Reid interaction with zero-range exchange term. This neglects physical effects included in other options, and so can be considered less realistic, however for comparison we present in Table VII the fusion barrier energies calculated using this latter parameter set too.

TABLE III. Parameters of the fusion barriers and the WS potentials which provide the best approximation to the DFP in the region of the calculated barrier. Calculations are performed for the M3Y-Paris potential, with $C_s=1/36$, and for either zero-range or finite-range exchange forces (δ or f in the first column). The type of density dependence (DD) is indicated in the second column (0 corresponds to the density-independent interaction). The R_B and B are the position and the height of the calculated barrier, V_{WS}, r_{WS}, and a_{WS} are the depth, the radius parameter, and the diffuseness of the WSP which approximates the DFP with an accuracy χ_R^2, defined by Eq. (18). The reaction is $^{12}C+^{92}Zr$, for which $B_{expt}=32.3$ MeV.

δ/f	DD label	R_B (fm)	B (MeV)	V_{WS} (MeV)	r_{WS} (fm)	a_{WS} (fm)	χ_R^2
δ		10.12	31.81	−66.2	1.16	0.67	3.6×10^{-5}
f	0	10.25	31.47	−171.8	1.08	0.67	8.2×10^{-5}
f	1	10.35	31.15	−88.2	1.16	0.67	5.9×10^{-5}
f	3	10.36	31.13	−152.5	1.10	0.68	6.4×10^{-5}
f	5	10.34	31.17	−88.3	1.16	0.67	4.1×10^{-5}
f	8	10.32	31.24	−120.6	1.12	0.68	1.3×10^{-5}

TABLE IV. The same as Table III, for the reaction ^{28}Si+^{92}Zr, for which B_{expt}=70.9 MeV.

δ/f	DD label	R_B (fm)	B (MeV)	V_{WS} (MeV)	r_{WS} (fm)	a_{WS} (fm)	χ^2_R
δ		10.58	70.97	−112.2	1.12	0.70	4.4×10^{-5}
f	0	10.73	70.17	−144.7	1.12	0.68	2.3×10^{-5}
f	1	10.81	69.57	−157.3	1.11	0.71	3.5×10^{-5}
f	3	10.81	69.57	−86.4	1.18	0.68	4.6×10^{-5}
f	5	10.80	69.62	−91.8	1.17	0.69	7.4×10^{-5}
f	8	10.79	69.73	−143.6	1.12	0.70	2.0×10^{-5}

In Fig. 10(b), the fractional differences between the experimental and calculated barriers are plotted, rather than the barriers themselves. This figure shows that on average the calculated Paris CDM3Y3 barrier energies are 2% lower than the measured ones. Since the height of the calculated fusion barrier depends weakly upon the type of the exchange interaction density dependence (see Fig. 7) this trend is a general one except for the unrealistic zero-range density-independent M3Y-Reid interaction barriers shown in Fig. 10(b) by crossed circles. This interaction gives the highest fusion barriers amongst all the interactions considered. To reproduce the empirical fusion barriers for this interaction would require a nuclear potential renormalization greater than unity. The same M3Y-Reid interaction was used in the analysis of elastic scattering with the microscopic optical model [9]. It is not surprising that this potential needed to be renormalized by a factor of typically 1.1, in qualitative agreement with the conclusions from the fusion barrier energies. From the low fusion barrier energies shown in Fig. 10(b) for the more realistic finite-range, density-dependent M3Y-Paris potential, it would seem reasonable that use of this potential in elastic scattering analysis would require renormalization factors less than unity. Such a factor is in disagreement with expectations that the potential renormalization due to couplings to high energy states should increase the nuclear attraction, as shown in Sec. IV A. It has however been claimed that the potential can become significantly less attractive as a result of couplings to breakup channels [30], in reactions of weakly bound nuclei. It would be interesting to see whether this effect is significant for the reactions involving heavy, well-bound nuclei considered here. This effect changes the potential renormalization, however a further mechanism exists that can change the bare potential. It has been shown [31] that the nuclear attraction can be reduced by 10–15% in the surface region due to the effects of Pauli blocking.

In conclusion, the empirical potential renormalizations from both analysis of elastic scattering and from comparison with fusion barrier energies seem to be in agreement, but depend strongly on the particular nucleon-nucleon interaction used. The more realistic interactions appear to give nuclear potentials with excessive strength, in view of the expectation that coupling to bound states results in a potential renormalization that increases the nuclear attraction. This suggests either that the double folding model is not appropriate for calculating the bare nucleus-nucleus potential without applying corrections due to Pauli blocking, and/or phenomena other than simple potential barrier penetration accompanied by coupling to collective states are involved in the fusion process. If the latter were the case, energy dissipation would seem a likely candidate. Reproduction of both the experimental fusion barrier energies and the apparent potential diffuseness must be achieved in a complete model of nuclear fusion.

C. Empirical potential diffuseness

Despite the problems in reconciling the strength of realistic DFM nuclear potentials with experiments, the DFM diffusenesses can be compared with those inferred from above-barrier fusion excitation functions, since the DFM diffuseness is rather insensitive to details of the nucleon-nucleon interaction, as seen from the results given in Tables III–VI. As will be illustrated later, the effective potential diffuseness depends mainly on the diffuseness of the nuclear matter distributions.

TABLE V. The same as Table III, for the reaction ^{16}O+^{92}Zr, for which B_{expt}=42.0 MeV.

δ/f	DD label	R_B (fm)	B (MeV)	V_{WS} (MeV)	r_{WS} (fm)	a_{WS} (fm)	χ^2_R
δ		10.22	41.97	−66.6	1.17	0.66	3.1×10^{-5}
f	0	10.36	41.52	−72.4	1.18	0.65	2.9×10^{-5}
f	1	10.45	41.13	−71.8	1.19	0.66	3.7×10^{-5}
f	3	10.45	41.11	−80.7	1.17	0.68	2.4×10^{-5}
f	5	10.44	41.15	−233.6	1.05	0.70	6.7×10^{-5}
f	8	10.42	41.24	−120.2	1.12	0.69	2.1×10^{-5}

TABLE VI. The same as Table III, for the reaction ^{16}O+^{144}Sm, for which B_{expt}=61.0 MeV.

δ/f	DD label	R_B (fm)	B (MeV)	V_{WS} (MeV)	r_{WS} (fm)	a_{WS} (fm)	χ^2_R
f	1	11.14	59.93	−86.2	1.17	0.69	1.2×10^{-5}
f	2	11.15	59.87	−105.2	1.15	0.70	5.5×10^{-5}
f	3	11.14	59.91	−78.2	1.18	0.69	7.2×10^{-5}
f	4	11.13	59.94	−72.7	1.19	0.68	8.7×10^{-5}
f	5	11.13	59.96	−148.0	1.11	0.71	3.3×10^{-5}
f	6	11.12	59.99	−162.1	1.10	0.71	4.3×10^{-5}
f	7	11.12	60.02	−137.2	1.12	0.70	4.2×10^{-5}
f	8	11.12	60.07	−168.4	1.10	0.70	5.5×10^{-5}

When fitting above-barrier fusion cross sections, the empirical diffuseness required is not completely independent of the WSP depth (or equivalently the radius parameter). However over a wide range of WSP depths, the empirical diffuseness for a given reaction typically varies by only 0.1 fm. For this reason, the values of a_{WS} taken from literature [6–8,30–33] have been assigned an uncertainty of ±0.1 fm. They are shown in Fig. 11 as a function of B_Z, for 13 reactions in which the heavy partner has no appreciable static deformation.

Before comparing the DFM predictions with the empirically determined diffuseness, the effects of channel couplings on the empirical diffuseness must also be considered. Calculations using CCFULL, for the ^{16}O+^{208}Pb reaction, show that the change in empirical diffuseness due to inclusion of different couplings is smaller than the assigned uncertainty of ±0.1 fm.

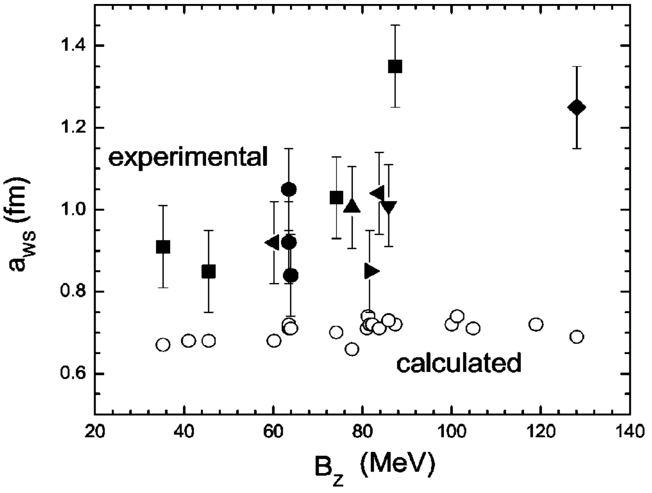

FIG. 11. The equivalent diffuseness of the DFP calculated for Paris finite-range CDM3Y3 interaction as a function of B_Z is shown by the open circles. Experimental values from fits to above-barrier fusion cross sections are indicated by the solid symbols, squares from Ref. [6], circles from Ref. [32], the triangle up from Ref. [7], triangles down from Ref. [33], triangles left from Ref. [34], triangle right from Ref. [35], and the diamond from Ref. [8].

Because of the relative insensitivity of the empirical diffuseness to other variables in the fits, values of a_{WS} from the literature will be compared directly with the equivalent diffuseness calculated with the DFM.

D. Fitting the double folding potential by a Woods-Saxon potential

To extract an equivalent diffuseness from the DFM nuclear potential, a Woods-Saxon potential was fitted to it in

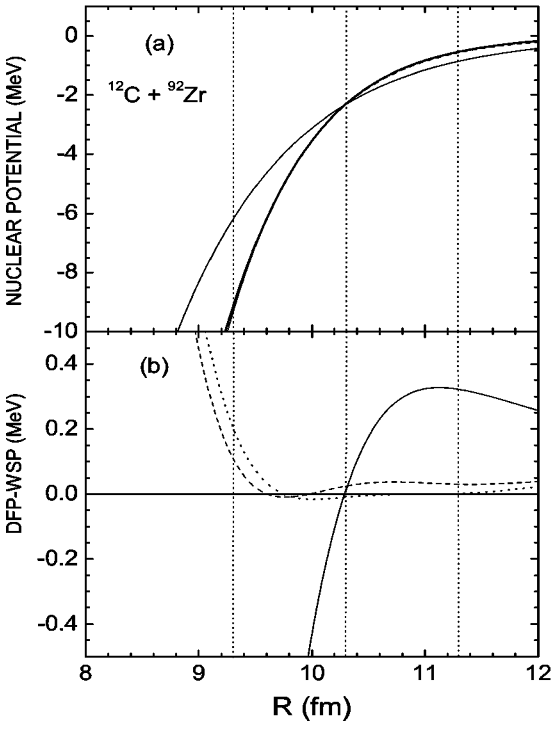

FIG. 12. (a) The nuclear potential calculated with the M3Y-Paris interaction with the density dependence 8 for the ^{12}C+^{92}Zr reaction (thick line) together with the fits obtained by minimizing the relative error (dotted line) and the absolute error (dashed line). The thin solid line is obtained by minimizing the relative error but by fixing the diffuseness a_{WS} to 1.00 fm. (b) The difference between the DFM potential and the Woods-Saxon fits. The middle vertical dotted line shows the barrier radius of the DFP, and the outer lines the boundaries of the fit region.

TABLE VII. Fusion barrier energies: B_{expt}—determined experimentally, $B_{R\delta}$—calculated using the M3Y-Reid interaction with zero-range exchange part, B_{Pf}—calculated using the Paris CDM3Y3 interaction with finite-range exchange part. The last four columns contain the radii and diffusenesses of the projectiles and targets. These parameters were either taken or scaled from either three-parameter Fermi profiles (3pF) or two-parameter Fermi profiles (2pF) from Table I of Ref. [22]. In the 3pF case the parameter w in Table I of Ref. [22] was taken to be equal to zero, and the proton (nucleon) densities were renormalized to $Z(A)$, respectively.

Reaction	B_{expt} (MeV)	$B_{R\delta}$ (MeV)	B_{Pf} (MeV)	R_P (fm)	a_P (fm)	R_T (fm)	a_T (fm)
^{12}C+^{92}Zr	32.3	32.03	31.15	2.441[a]	0.456[a]	4.913[b]	0.533[b]
^{9}Be+^{208}Pb	38.2	38.94	38.05	2.218[a]	0.458[a]	6.631[c]	0.505[c]
^{16}O+^{92}Zr	42.0	42.26	41.14	2.608[d]	0.465[d]	4.913[b]	0.533[b]
^{12}C+^{204}Pb	57.6	58.61	57.30	2.441[a]	0.456[a]	6.588[e]	0.504[e]
^{16}O+^{148}Sm	59.8	61.19	59.61	2.608[d]	0.465[d]	5.771[f]	0.558[f]
^{17}O+^{144}Sm	60.6	61.10	59.53	2.661[g]	0.466[g]	5.719[h]	0.557[h]
^{16}O+^{144}Sm	61.0	61.53	59.94	2.608[d]	0.465[d]	5.719[h]	0.557[h]
^{28}Si+^{92}Zr	70.9	71.46	69.59	3.140[f]	0.491[f]	4.913[b]	0.533[b]
^{16}O+^{208}Pb	74.5	77.08	75.40	2.608[d]	0.465[d]	6.631[c]	0.505[c]
^{36}S+^{96}Zr	76.7	77.65	75.45	3.509[i]	0.560[i]	4.922[b]	0.533[b]
^{34}S+^{89}Y	76.9	77.55	75.42	3.443[i]	0.559[i]	4.860[f]	0.499[f]
^{32}S+^{89}Y	77.8	78.21	76.04	3.374[i]	0.558[i]	4.860[f]	0.499[f]
^{36}S+^{90}Zr	78.0	78.26	76.01	3.509[i]	0.560[i]	4.878[b]	0.532[b]
^{19}F+^{197}Au	80.8	83.83	81.90	2.580[f]	0.525[f]	6.380[f]	0.493[f]
^{35}Cl+^{92}Zr	82.9	83.57	81.15	3.476[d]	0.559[d]	4.913[b]	0.533[b]
^{19}F+^{208}Pb	83.0	85.26	83.25	2.580[f]	0.525[f]	6.631[c]	0.505[c]
^{40}Ca+^{96}Zr	94.6	97.01	94.32	3.766[d]	0.544[d]	4.922[b]	0.533[b]
^{40}Ca+^{90}Zr	96.9	97.78	95.01	3.766[d]	0.544[d]	4.878[b]	0.532[b]
^{28}Si+^{144}Sm	104.0	104.37	101.72	3.140[f]	0.491[f]	5.719[h]	0.557[h]
^{40}Ca+^{124}Sn	113.1	117.89	114.96	3.766[d]	0.544[d]	5.490[f]	0.492[f]
^{28}Si+^{208}Pb	128.1	130.90	128.08	3.140[f]	0.491[f]	6.631[c]	0.505[c]

[a] R_P was scaled from 3pF ^{14}N, a_P was taken to be the same as for 3pF ^{14}N.

[b] R_P was scaled from 2pF ^{93}Nb, a_P was taken to be the same as for 2pF ^{93}Nb.

[c] R_P was scaled from 2pF ^{207}Pb, a_P was taken to be the same as for 2pF ^{207}Pb.

[d] Taken from 3pF.

[e] R_P was scaled from 2pF ^{206}Pb, a_P was taken to be the same as for 2pF ^{206}Pb.

[f] Taken from 2pF.

[g] R_P was scaled from 3pF ^{16}O, a_P was taken to be the same as for 3pF ^{16}O.

[h] R_P was scaled from 2pF ^{148}Sm, a_P was taken to be the same as for 2pF ^{148}Sm.

[i] R_P was scaled from 3pF ^{35}Cl, a_P was taken to be the same as for 3pF ^{35}Cl.

the region of the fusion barrier. In order to estimate the quality of the fit one can calculate a relative error

$$\chi_R^2 = \frac{1}{N}\sum_{i=1}^{N}\left(\frac{U_{DF}(R_i)-U_{WS}(R_i)}{U_{DF}(R_i)+U_{WS}(R_i)}\right)^2 \qquad (18)$$

for distances R_i around the fusion barrier radius R_B, over the range $R_B-1\ \text{fm}<R_i<R_B+1$ fm with a step of 0.01 fm. The parameters of the WSP were allowed to vary within the following ranges, with steps as shown: $2|U_{DF}(0)|>|V_{WS}|>20$ MeV, $\Delta V_{WS}=20$ MeV; 1.2 fm $<r_{WS}<0.8$ fm, $\Delta r_{WS}=0.01$ fm; 0.5 fm$<a_{WS}<1.2$ fm, $\Delta a_{WS}=0.01$ fm. Here $U_{DF}(0)$ is the depth of the double folding potential at $R=0$. The WSP obtained using this method is denoted by WSR.

An alternative option is to minimize an absolute error

$$\chi_A^2 = (1/N)\sum_{i=1}^{N}[U_{DF}(R_i)-U_{WS}(R_i)]^2 \qquad (19)$$

varying the parameters of the WSP as above. The WSP obtained by this fit is denoted by WSA.

In order to obtain the best WSP for a fixed diffuseness we performed a third fit. Here the error was estimated using Eq. (18) but the diffuseness was fixed to be $a_{WS}=1.00$ fm. The WSP resulting from this constrained fit is called WSC.

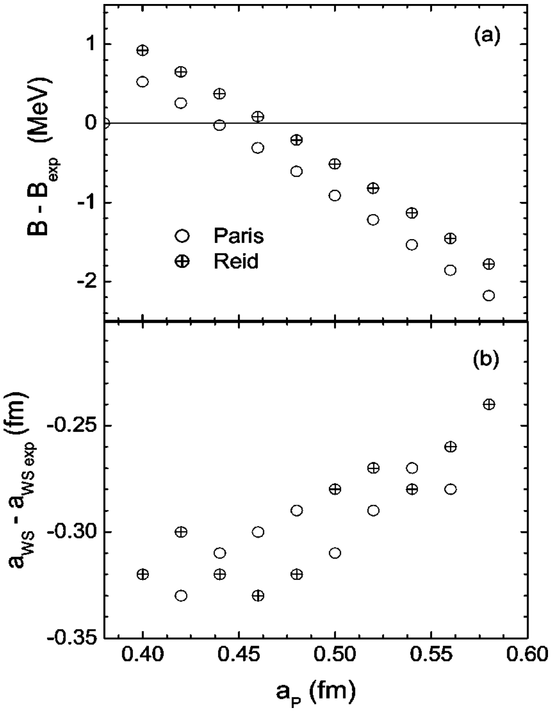

FIG. 13. (a) The difference between the calculated barrier energies and experiment for the $^{16}O+^{144}Sm$ reaction, as a function of the diffuseness of the ^{16}O nucleon distribution. The difference between the equivalent fitted WSP diffuseness and experiment are shown in (b). The experimental barrier energy and empirical diffuseness cannot be simultaneously reproduced.

The quality of these three WSP fits to the DFM potential is shown in Fig. 12, for the $^{12}C+^{92}Zr$ reaction. In the upper panel the nuclear potentials are shown. The relative error fit (WSR) with $a_{WS}=0.74$ fm, $V_{WS}=-179.4$ MeV, $r_{WS}=1.07$ fm is shown by the dotted line, while that for the absolute error (WSA) is shown by the dashed line, having the parameters $a_{WS}=0.75$ fm, $V_{WS}=-119.4$ MeV, $r_{WS}=1.11$ fm. They both provide a very good approximation to the DFP (thick full line), WSA in particular being hardly distinguishable from the DFP. The thin solid line corresponds to the constrained fit WSC with $a_{WS}=1.00$ fm (not varied), $V_{WS}=-258.1$ MeV, $r_{WS}=0.80$ fm. It coincides with the DFP at the barrier radius (middle vertical dotted line) but deviates significantly from the DFP in the region of fit, the latter indicated by the outer vertical dotted lines.

Figure 12(b) shows the difference between the DFP and the Woods-Saxon fits described above. The quality of fit with WSR is very good, the maximum deviation being only 0.2 MeV. WSA approximates the DFP even better near the left border of the region of the fit.

It is concluded that DFM potentials can be very well described by a Woods-Saxon potential form, from nuclear separations 1 fm inside the fusion barrier radius, up to large separations. Thus the discrepancy between diffusenesses obtained from fitting elastic scattering data and from above-barrier fusion data is not due to the WS potential being inadequate to describe the semimicroscopic DFM potential. The discrepancy must arise from more fundamental reasons.

E. Equivalent diffuseness of the DFM potential

The parameters of the WSP providing the best fit (WSR) for the calculated DFP, as well as the corresponding values of χ_R^2, are presented in Tables III–VI for a number of the reactions. Neither with zero-range nor with finite-range exchange forces does the DFM give the large values of the equivalent diffuseness of about 1 fm, as obtained by analysis of the high energy experimental fusion cross sections. In almost all cases, the equivalent diffuseness is between 0.65 and 0.70 fm.

To provide a general picture of the equivalent diffuseness of the DFM nuclear potential, the fitted diffuseness values as a function of B_Z are compared with empirical values in Fig. 11. Calculations were performed here for all 21 systems of Table VII, using finite-range Paris forces with the CDM3Y3 density dependence. The experimental results lie well above the calculated values.

The effect of changes in the diffuseness of the nucleon density distributions must be investigated, as a_P and a_T were often scaled from neighboring measurements. With this aim, calculations were made with zero-range M3Y-Paris and Reid interactions for the $^{16}O+^{144}Sm$ reaction. Results of this calculation are shown as a function of a_P in Fig. 13. The diffuseness of the projectile proton (nucleon) distribution was varied from 0.40 fm up to 0.58 fm; the value available in the literature is 0.45 fm (Ref. [24]). In Fig. 13(a) the difference between these calculated barriers and experiment, $B-B_{expt}$, is plotted. In Fig. 13(b) the difference between the diffuseness of WSR and the experimental value is shown. Only very small values of a_P can make the calculated barrier significantly higher than the experimental one. However the experimentally determined diffuseness cannot be reproduced even with very large values of the a_P.

In summary, it is impossible to simultaneously reproduce the expected barrier energy and the experimentally determined potential diffuseness through variation of the diffuseness of the nucleon density distributions. As might be expected, the use of different forms of nucleon-nucleon effective interaction (M3Y-Reid or Paris, zero range or finite range, density independent or dependent) hardly affects the diffuseness required to reproduce the DFM potential.

V. CONCLUSIONS

This paper has addressed the following questions: what are the predictions of a semimicroscopic double folding model for fusion barrier energies and the nuclear potential diffusenesses? Can these show whether the DFM potential is appropriate to be used as the bare potential in coupled-channels calculations? To answer these questions, a computer code was developed that calculates the double folding nuclear and Coulomb potentials for two spherical colliding nuclei. The code uses the M3Y nucleon-nucleon interaction with a finite-range density-dependent exchange part and the extended Thomas-Fermi approximation for the effective Fermi momentum in the density matrix expansion. Calculations were performed for 21 reactions for which accurate experimental fusion barriers are available.

The M3Y-Paris density-dependent *NN* interaction which reproduces the basic properties of nuclear matter results in fusion barrier energies that are systematically lower than the measured barriers. *A priori* an opposite result was expected, since the experimental barriers are reduced, typically by several percent, due to coupling to collective states at high excitation energy which renormalize the potential barriers. Only the M3Y-Reid interaction with zero-range exchange term results in barrier energies that are larger than the experimental values. However this parameter set of the M3Y interaction has been shown to fail in saturating cold nuclear matter.

The diffuseness of the equivalent Woods-Saxon potential fitted to the DFP in the fusion barrier region is typically 0.65–0.70 fm, and this reproduces the shape of the DFP very well. The DFP cannot be reproduced by a WSP with a diffuseness of ~1.0 fm, which is required empirically to fit the above-barrier fusion cross-section excitation functions for many of the reactions. The semimicroscopic calculations in general predict bare fusion barriers and nuclear potential diffusenesses which are lower than those deduced from experimental fusion cross sections.

At the moment we see two possible causes for this disagreement. The first is that the DFM with the M3Y interactions does not correctly predict the bare nucleus-nucleus potential at the fusion barrier radius, which may be related to the frozen density approximation. This conclusion, if correct, would have implications for other uses of these calculated nuclear potentials in interpretation of heavy-ion collisions. The second possibility is energy dissipation. This could cause the higher average fusion barrier energies through kinetic energy loss to dissipation, and the apparent large potential diffuseness through the larger energy dissipation that would be expected for high angular momentum, where the barrier peak occurs at smaller separation and thus larger nuclear overlap.

A comprehensive model which includes dissipative effects and channel couplings, which to our knowledge does not yet exist, is likely to give insight into the possible role of energy dissipation in fusion reactions near the barrier.

The present work indicates that potential renormalization from coupling to high energy collective states can be so large that the nuclear potentials calculated with the double folding model using realistic M3Y interactions are much too attractive, unless substantial dissipation of kinetic energy is invoked before the fusion barrier radius is reached. Further theoretical and experimental studies on these questions are necessary to resolve this discrepancy.

ACKNOWLEDGMENTS

We are grateful to Dao T. Khoa for valuable remarks, and to K. Hagino, A. Mukherjee, C.R. Morton, and R.D. Butt for fruitful discussions. I.I.G. acknowledges the warm hospitality of the Department of Nuclear Physics of the RSPhysSE, ANU.

[1] C. H. Dasso, S. Landowne, and A. Winther, Nucl. Phys. **A405**, 381 (1983); **A407**, 221 (1983).
[2] M. Dasgupta, D. J. Hinde, N. Rowley, and A. M. Stefanini, Annu. Rev. Nucl. Part. Sci. **48**, 401 (1998).
[3] R. Bass, Phys. Rev. Lett. **39**, 265 (1977).
[4] C. Y. Wong, Phys. Rev. Lett. **31**, 766 (1973).
[5] N. Rowley, A. Kabir, and R. Lindsay, J. Phys. G **15**, L269 (1989).
[6] J. O. Newton, C. R. Morton, M. Dasgupta, J. R. Leigh, J. C. Mein, D. J. Hinde, H. Timmers, and K. Hagino, Phys. Rev. C **64**, 064608 (2001).
[7] C. R. Morton, A. C. Berriman, M. Dasgupta, D. J. Hinde, J. O. Newton, K. Hagino, and I. J. Thompson, Phys. Rev. C **60**, 044608 (1999).
[8] D. J. Hinde, C. R. Morton, M. Dasgupta, J. R. Leigh, J. C. Mein, and H. Timmers, Nucl. Phys. **A592**, 271 (1995).
[9] G. R. Satchler and W. G. Love, Phys. Rep. **55**, 183 (1979).
[10] K. Hagino, M. Dasgupta, I. I. Gontchar, D. J. Hinde, C. R. Morton, and J. O. Newton, ANU Report No. P/1500, 2001 (unpublished).
[11] Dao T. Khoa, Phys. Rev. C **63**, 034007 (2001).
[12] Dao T. Khoa, W. von Oertzen, and H. G. Bohlen, Phys. Rev. C **49**, 1652 (1994).
[13] Dao T. Khoa and G. R. Satchler, Nucl. Phys. **A668**, 3 (2000).
[14] G. Bertsch, J. Borysowicz, H. McManus, and W. G. Love, Nucl. Phys. **A284**, 399 (1977).
[15] N. Anantaraman, H. Toki, and G. F. Bertsch, Nucl. Phys. **A398**, 269 (1983).
[16] Dao T. Khoa and W. von Oertzen, Phys. Lett. B **304**, 8 (1993).
[17] M. Ismail and Kh. A. Ramadan, J. Phys. G **26**, 1621 (2000).
[18] Dao T. Khoa, G. R. Satchler, and W. von Oertzen, Phys. Rev. C **56**, 954 (1997).
[19] J. W. Negele and D. Vautherin, Phys. Rev. C **5**, 1472 (1972).
[20] X. Campi and A. Bouyssy, Phys. Lett. B **73**, 263 (1978).
[21] A. M. Kobos, B. A. Brown, R. Lindsay, and G. R. Satchler, Nucl. Phys. **A425**, 205 (1984).
[22] H. de Vries, C. W. de Jager, and C. de Vries, At. Data Nucl. Data Tables **36**, 495 (1987).
[23] R. Hasse and W. J. Myers, *Geometrical Relationships in Nuclear Physics* (Springer-Verlag, Berlin, 1988), pp. 23 and 31.
[24] M. El-Azab Farid and G. R. Satchler, Nucl. Phys. **A438**, 525 (1985).
[25] Dao T. Khoa, W. von Oertzen, H. G. Bohlen, G. Bartnitzky, H. Clement, Y. Sugiyama, B. Gebauer, A. N. Ostrowski, Th. Wilpert, M. Wilpert, and C. Langner, Phys. Rev. Lett. **74**, 34 (1995).
[26] K. Hagino, N. Takigawa, M. Dasgupta, D. J. Hinde, and J. R. Leigh, Phys. Rev. Lett. **79**, 2014 (1997).
[27] K. Hagino, N. Rowley, and A. T. Kruppa, Comput. Phys. Commun. **123**, 143 (1999).
[28] C. H. Dasso and S. Landowne, Comput. Phys. Commun. **46**, 187 (1987); J. O. Fernandez Niello, C. H. Dasso, and S. Landowne, *ibid.* **54**, 409 (1989).

[29] M. Dasgupta, A. Navin, Y. K. Agarwal, C. V. K. Baba, H. C. Jain, M. L. Jhingan, and A. Roy, Nucl. Phys. **A539**, 351 (1992).
[30] Y. Sakuragi, Phys. Rev. C **35**, 2161 (1987).
[31] V. B. Soubbotin, W. von Oertzen, X. Vinas, K. A. Gridnev, and H. G. Bohlen, Phys. Rev. C **64**, 014601 (2001).
[32] J. R. Leigh, M. Dasgupta, D. J. Hinde, J. C. Mein, C. R. Morton, R. C. Lemmon, J. P. Lestone, J. O. Newton, H. Timmers, J. X. Wei, and N. Rowley, Phys. Rev. C **52**, 3151 (1995).
[33] D. J. Hinde, A. C. Berriman, M. Dasgupta, J. R. Leigh, J. C. Mein, C. R. Morton, and J. O. Newton, Phys. Rev. C **60**, 054602 (1999).
[34] A. C. Berriman, Ph.D. thesis, ANU, 2001.
[35] A. Mukherjee, M. Dasgupta, D. J. Hinde, K. Hagino, J. R. Leigh, J. C. Mein, C. R. Morton, J. O. Newton, and H. Timmers, Phys. Rev. C **66**, 034607 (2002).